Multiorbital exciton formation in an organic semiconductor

Wiebke Bennecke,¹ Andreas Windischbacher,² David Schmitt,¹ Jan Philipp Bange,¹ Ralf Hemm,³ Christian S. Kern,² Gabriele D'Avino,⁴ Xavier Blase,⁴ Daniel Steil,¹ Sabine Steil,¹ Martin Aeschlimann,³ Benjamin Stadtmüller,^{3,5} Marcel Reutzel,¹ Peter Puschnig,² G. S. Matthijs Jansen,^{1,*} and Stefan Mathias^{1,6,†}

¹I. Physikalisches Institut, Georg-August-Universität
Göttingen, Friedrich-Hund-Platz 1, 37077 Göttingen, Germany

²Institute of Physics, University of Graz, NAWI
Graz, Universitätsplatz 5, 8010 Graz, Austria

³Department of Physics and Research Center OPTIMAS, University of
Kaiserslautern, Erwin-Schrödinger-Straβe 46, 67663, Kaiserslautern, Germany

⁴Univ. Grenoble Alpes, CNRS, Inst NEEL, F-38042 Grenoble, France

⁵Institute of Physics, Johannes Gutenberg-University Mainz, 55128 Mainz, Germany

⁶International Center for Advanced Studies of Energy Conversion
(ICASEC), University of Göttingen, Göttingen, Germany

(Dated: March 27, 2023)

Abstract

Harnessing the optoelectronic response of organic semiconductors requires a thorough understanding of the fundamental light-matter interaction that is dominated by the excitation of correlated electron-hole pairs, i.e. excitons. The nature of these excitons would be fully captured by knowing the quantum-mechanical wavefunction, which, however, is difficult to access both theoretically and experimentally. Here, we use femtosecond photoemission orbital tomography in combination with many-body perturbation theory to gain access to exciton wavefunctions in organic semiconductors. We find that the coherent sum of multiple electron-hole pair contributions that typically make up a single exciton can be experimentally evidenced by photoelectron spectroscopy. For the prototypical organic semiconductor buckminsterfullerene (C_{60}), we show how to disentangle such multiorbital contributions and thereby access key properties of the exciton wavefunctions including localization, charge-transfer character, and ultrafast exciton formation and relaxation dynamics.

I. MAIN

Excitons, quasiparticles consisting of bound electron-hole pairs, are at the heart of the optoelectronic response of all organic semiconductors, and exciton formation and relaxation processes are largely responsible for energy conversion and light harvesting applications in these materials. At the atomic level, excitons are described by a two-particle correlated quantum-mechanical wavefunction that includes both the excited electron and the remaining hole. This wavefunction covers the complete shape of the exciton wave and thus provides access to a number of critical exciton properties such as the orbital character, the degree of (de)localization, the degree of charge separation, and whether this involves charge transfer between molecules. Consequently, in order to fully understand exciton dynamics and to exploit them in, e.g., an organic solar cell, an accurate and complete measurement of the exciton wavefunction would be ideal. Exemplary in this situation is the ongoing work to understand the optoelectronic response of C₆₀, a prototypical organic semiconductor that is commonly used in organic solar cells¹⁻³. Here, a topic of research has been the optical absorption feature that occurs at 2.8 eV for multilayer and other aggregated structures of C_{60}^{4} . Interestingly, time- and angle-resolved photoelectron spectroscopy and optical absorption spectroscopy studies have indirectly found that this optical transition corresponds to the formation of charge-transfer excitons with significant electron-hole separation^{5–9}. Although these hints are supported by time-dependent density functional theory calculations that show the importance of delocalized excitations in C_{60} clusters $^{10-12}$, quantitative measurements of the exciton localization and charge separation have so far not been possible. Thus, the C_{60} case highlights the need for a more direct experimental access to the wavefunctions of the electron-hole pair excitations.

From an experimental point of view, our method of choice to access exciton wavefunctions is time-resolved photoemission orbital tomography (tr-POT, see Methods for the experimental realization used in this work)^{13–16}. In POT, the comparison with density functional theory calculations (DFT) provides a direct connection between photoemission data and the orbitals of the electrons.¹³ The extension to the time-domain promises valuable access also to the spatial information of excited electrons. However, at least for organic semiconductors, it has not been explicitly considered that photoemission of excitons requires the break-up of the two-particle electron-hole pair and that only the photoemitted electron, but

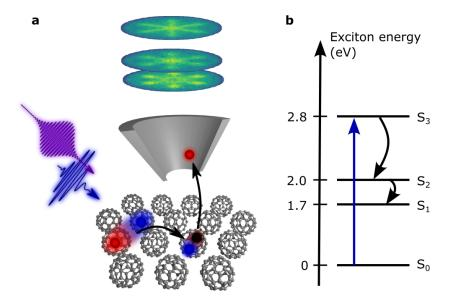


FIG. 1. Schematic overview of time-resolved photoemission orbital tomography of exciton states in C_{60} . **a, b**, a femtosecond optical pulse (blue pulse and blue arrow in (**a**) and (**b**), respectively) excites optically bright excitons in a C_{60} film. The exciton electron-hole pairs are sketched in (**a**) as correlated particles (shaded blue-red areas) with a blue sphere for the hole and a red sphere for the electron. We probe the excitons in C_{60} with extreme ultraviolet (EUV) pulses (purple pulse in (**a**), $h\nu = 26.5$ eV) that break up the electron-hole pairs and photoemit the corresponding electrons (red spheres), of which we detect the kinetic energies and the momentum emission patterns (yellow-green-colored disks in (**a**)). The optical excitation of excitons in C_{60} is known to lead to the formation of a decay sequence of singlet exciton states with varying charge-transfer character^{5,6} (see (**b**), S_i : ith singlet excited state, S_0 : ground state). We are able to measure these exciton dynamics and the corresponding orbital tomography momentum patterns by adjusting the temporal delay between the optical excitation and the EUV probe pulses.

not the hole, is directly detected. In fact, it is not clear to what extent (tr-)POT can be reasonably used for the interpretation and analysis of such strongly interacting correlated quasiparticles. Here we address this open question and show how tr-POT can probe the exciton wavefunction in the example system of a C_{60} multilayer.

We employ our recently developed setup for photoelectron momentum microscopy^{17–19} and use ultrashort laser pulses to optically excite bright excitons in C_{60} thin films that were deposited on Cu(111) (measurement temperature $T \approx 80$ K; see Methods and Figure 1a). In

the time-resolved photoemission experiment, we detect the energy and momentum emission pattern of the photoemitted electrons, which were initially part of the bound electron-hole pairs, i.e. the excitons. Following the time-evolution of the photoelectron spectrum, we can observe how the optically excited states relax to energetically lower-lying dark exciton states with different localization and charge-transfer character^{5,6} (Figure 1b and data in Extended Fig. 6). In addition to the energy relaxation, we collect tr-POT data, and investigate in how far these patterns can be used to access real-space properties of the exciton wavefunctions. Specifically, we will address two questions: which orbitals contribute to the formation of the excitons and how this key information is imprinted in the energy- and momentum-resolved photoemission spectra.

II. RESULTS & DISCUSSION

A. The exciton spectrum of buckminsterfullerene C_{60}

To lay the foundation for our study, we first discuss the theoretical electronic properties of the C_{60} film. On top of a hybrid-functional DFT ground state calculation, we obtain the exciton spectrum by employing the many-body framework of GW and Bethe-Salpeter-Equation (GW+BSE) calculations (see Methods for full details). As shown in Fig. 2a, we model the C_{60} low-temperature phase by the two symmetry-inequivalent C_{60} dimers 1-2 and 1-4, respectively²⁰, which are properly embedded to account for polarization effects in the film. The calculated single-particle energy levels are shown in Fig. 2b, where we group the electron removal and electron addition energies into four bands, denoted as HOMO-1, HOMO, LUMO, and LUMO+1 according to the orbitals of the parent orbitals of an gasphase C_{60} molecule. These manifolds consist of 18, 10, 6, and 6 energy levels per dimer, respectively, originating from the g_g+h_g , h_u , t_{1u} , and t_{1g} irreducible representations of the gas phase C_{60} orbitals²¹. We emphasize that the calculated GW ionization levels of HOMO and HOMO-1 of 6.7 eV and 8.1 eV are in excellent agreement with experimental data for this C_{60} film (see SI and Ref. 22).

Building upon the GW single-particle energies, we solve the Bethe-Salpeter equation and compute the energies Ω_m of all correlated electron-hole pairs (excitons). The resulting absorption spectrum (bottom panel of Fig. 2c) agrees well with literature⁴. In addition,

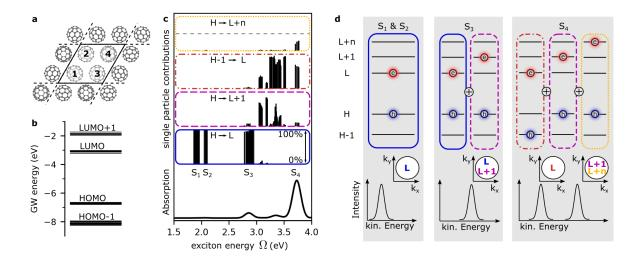


FIG. 2. Ab-initio calculation of the electronic structure and exciton spectrum of C_{60} dimers in a crystalline multilayer sample. **a**, the unit cell for a monolayer of C_{60} , for which GW+BSE calculations for the dimers 1-2 and 1-4 were performed. **b**, electron addition/removal single-particle energies as retrieved from the self-consistent GW calculation. These energies directly provide ε_v in Eq. (2). **c**, results of the full GW+BSE calculation, showing as a function of the exciton energy Ω from bottom to top: the calculated optical absorption, the exciton band assignment $S_1 - S_4$, and the relative contributions to the exciton wavefunctions of different electron-hole pair excitations $\phi_v(\mathbf{r}_h)\chi_c(\mathbf{r}_e)$. Full details on the calculations are given in the Methods section. **d**, sketch of the composition of the exciton wavefunction of the $S_1 - S_4$ bands and their expected photoemission signatures based on Eq. (2). In order to visualize the contributing orbitals, blue holes and red electrons are assigned to the single-particle states as shown in (b).

we obtain the weights $X_{vc}^{(m)}$ on the specific electron-hole pairs that coherently contribute to the m^{th} exciton state, from which the exciton wavefunctions are constructed in the Tamm-Dancoff approximation as follows:

$$\psi_m(\mathbf{r}_h, \mathbf{r}_e) = \sum_{v,c} X_{vc}^{(m)} \phi_v^*(\mathbf{r}_h) \chi_c(\mathbf{r}_e). \tag{1}$$

This means that each exciton ψ_m with energy Ω_m consists of a weighted coherent sum of multiple electron-hole-transitions $\phi_v(\mathbf{r}_h)\chi_c(\mathbf{r}_e)$ each containing one electron orbital χ_c and one hole orbital ϕ_v .

To gain more insight into the character of the excitons ψ_m , we qualitatively classify them according to the most dominant orbital contributions that are involved in the transitions.

This is visualized in the four sub-panels above the absorption spectrum in Fig. 2c. For a given exciton energy Ω_m , the black bars in each sub-panel show the partial contribution $|X_{v,c}^{(m)}|^2$ of characteristic electron-hole transitions $\phi_v(\mathbf{r}_h)\chi_c(\mathbf{r}_e)$ to a given exciton ψ_m . Looking at individual sub-panels, we see first that characteristic electron-hole transitions can belong to different excitons ψ_m that have very different exciton energies Ω_m . For example, the blue panel in Fig. 2c shows the contributions of HOMO \rightarrow LUMO (abbreviated H \rightarrow L) transitions as a function of exciton energy Ω_m , and we see that these transitions contribute to excitons that are spread in energy over a scale of more than 1 eV (from $\Omega_m \approx 1.7$ eV to 3 eV). This spread of H \rightarrow L contributions (and also H-n \rightarrow L+m contributions) is caused by the fact that there are already many orbital energies per dimer (cf. Fig. 2b) which combine to form excitons with different degrees of localization and delocalization of the electrons and holes on one or more molecules.

We now focus on four exciton bands of the C_{60} film, denoted as S_1 - S_4 , which are centered around Ω_{S1} , Ω_{S2} , Ω_{S3} and Ω_{S4} at 1.9, 2.1, 2.8 and 3.6 eV, respectively (cf. Ref. 6). It is important to emphasize that each exciton band S_1 - S_4 arises from many individual excitons ψ_m with similar exciton energies Ω_m within the exciton band. Looking again at the subpanels, we see that the S_1 and S_2 exciton bands are made up of excitons ψ_m that are almost exclusively composed of transitions from $H\rightarrow L$. On the other hand, the S_3 shows in addition to $H\rightarrow L$ also significant contributions from $H\rightarrow L+1$ transitions (pink-dashed panel). The S_4 exciton band can be characterized as arising from $H\rightarrow L+1$ (pink-dashed panel) and $H-1\rightarrow L$ (orange-dash-dotted panel) as well as transitions from the HOMO to several higher lying orbitals denoted as $H\rightarrow L+n$ (yellow-dotted panel). We emphasize that although orbitals from several different GW energies contribute, e.g., to an exciton in the S_4 band, the exciton energy Ω_m of each exciton ψ_m has a single well-defined value.

B. Photoemission signatures of multiorbital contributions

In the following, we investigate whether these theoretically predicted multiorbital characteristics of the excitons can also be probed experimentally. As will be shown below, time-resolved photoemission spectroscopy can indeed provide access not only to the dark exciton landscape^{23–27}, but also to the distinct orbital contributions of exciton states. A key step in extracting this information from the experimental data lies in a thorough compar-

ison with simulations that specifically consider the pump-probe photoemission process, a topic that has recently attracted increased attention^{28–31}. Here, we rely on the formalism of Kern *et al.*³², which is based on a common Fermi's golden rule approach to photoemission³³. Assuming the exciton of Eq. (1) as the initial state and applying the plane-wave final state approximation of POT, the photoemission intensity of the exciton ψ_m is formulated as

$$I_m(E_{\rm kin}, \mathbf{k}) \propto |\mathbf{A}\mathbf{k}|^2 \sum_{v} \left| \sum_{c} X_{vc}^{(m)} \mathcal{F} \left[\chi_c \right] (\mathbf{k}) \right|^2 \times \delta \left(h\nu - E_{\rm kin} - \varepsilon_v + \Omega_m \right).$$
 (2)

Here \mathbf{A} is the vector potential of the incident light field, \mathcal{F} the Fourier transform, \mathbf{k} the photoelectron momentum, $h\nu$ the probe photon energy, ε_v the v^{th} ionization potential, Ω_m the exciton energy, and E_{kin} the energy of the photoemitted electron. Note that ε_v directly indicates the final-state energy of the left-behind hole. In the context of our present study, delving into Eq. (2) leads to two striking consequences, which we discuss in the following.

First, we illustrate the consequences of the multiorbital character of the exciton states on the photoelectron spectrum, and sketch in Fig. 2d the typical single-particle energy level diagrams for the HOMO and LUMO states and then indicate the contributing orbitals to the two-particle exciton state by blue holes and red electrons in these states, respectively. For the S₁ exciton band (left panel), we already found that the main orbital contributions to the band are of H \rightarrow L character (Fig. 2d, left, and cf. Fig. 2c, blue panel). To determine the kinetic energy of the photoelectrons originating from the exciton, we have to consider the correlated nature of the electron-hole pair. The energy conservation expressed by the delta function in Eq. 2 (see also Ref. 23 and 34) requires that the kinetic energy of the photoelectron depends on the ionization energy of the involved HOMO hole state $\varepsilon_v = \varepsilon_H$ and the correlated electron-hole pair energy $\Omega \approx \Omega_{S_1}$. Therefore, we expect to measure a single photoelectron peak, as shown in the lower part of the left panel of Fig. 2d. In the case of the S₂ exciton the situation is similar, since the main orbital contributions are also of H \rightarrow L character. However, since the S₂ exciton band has a different energy Ω_{S_2} , the photoelectron peak is located at a different kinetic energy with respect to the S₁ peak.

In the case of the S_3 exciton band, we find that in contrast to the S_1 and S_2 excitons not only $H\rightarrow L$, but also $H\rightarrow L+1$ transitions contribute (Fig. 2d, middle panel, and cf. Fig 2c, blue and pink-dashed panels, respectively). However, we still expect a single peak in the photoemission, because the same hole states are involved for both transitions (i.e., same $\varepsilon_v = \varepsilon_H$ in the sum in Eq. 2), and all orbital contributions have the same exciton

energy $\approx \Omega_{S_3}$, even though transitions with electrons in energetically very different single-particle LUMO and LUMO+1 states contribute. With other words, and somewhat counter-intuitively, the single-particle energies of the electron orbitals (the LUMOs) contributing to the exciton do not enter the energy conservation term in Eq. 2, and thus do not affect the kinetic energy observed in the experiment.

Finally, for the S_4 exciton band at $\Omega_{S4}=3.6$ eV, we find three major contributions (Fig. 2d, right panel), where not only the electrons but also the holes are distributed over two energetically different levels, namely the HOMO (cf. pink-dashed and yellow-dotted panels in Fig. 2c,d) and the HOMO-1 (cf. orange-dash-dotted panels in Fig. 2c,d). Thus, there are two different final states available for the hole, each with a different binding energy. Consequently, the photoemission spectrum of S_4 is expected to exhibit a double-peak structure with intensity appearing ≈ 3.6 eV above the HOMO kinetic energy E_H , and ≈ 3.6 eV above the HOMO-1 kinetic energy E_{H-1} , as illustrated in the right-most panel of Fig. 2d. Relating this specifically to the single-particle picture of our GW calculations, the two peaks are predicted to have a separation of $\varepsilon_{H-1} - \varepsilon_H = 8.1 - 6.7 = 1.4$ eV.

In addition, Eq. (2) now also provides the theoretical framework for interpreting momentum-resolved tr-POT data from excitons. Ground state POT can be easily understood in terms of the Fourier transform \mathcal{F} of single-particle orbitals. A naive extension to excitons might imply an incoherent, weighted sum of all LUMO orbitals χ_c contributing to the exciton wavefunction. However, as Eq. (2) shows, such a simple picture proves insufficient. Instead, the momentum pattern of the exciton wavefunction is related to a coherent superposition of the electron orbitals χ_c weighted by the electron-hole coupling coefficients $X_{vc}^{(m)}$. The implications of this finding are sketched in the k_x - k_y plots in Fig. 2d and are most obvious for the S₃ band. Here, the exciton is composed of transitions with a common hole position, i.e., $H\rightarrow$ L and $H\rightarrow$ L+1, leading to a coherent superposition of all 12 electron orbitals from the LUMO and LUMO+1 in the momentum distribution. In summary, multiple hole contributions can be identified in a multi-peak structure in the photoemission spectrum, and multiple electron contributions will result in a coherent sum of the electron orbitals that can be identified in the corresponding energy-momentum patterns from tr-POT data.

C. Disentangling multiorbital contributions experimentally

These very strong predictions about multi-peaked photoemission spectra due to multiorbital excitons can be directly verified in an experiment on C_{60} by comparing spectra for resonant excitation of either the S_3 or the S_4 excitons (cf. Fig. 2). The corresponding experimental data are shown in Fig. 3a and 3c, respectively. Starting from the excitation of the S_3 exciton band with $h\nu = 2.9$ eV photon energy (which is sufficiently resonant to excite the manifold of exciton states that make up the S_3 band around $\Omega_{S_3} = 2.8$ eV), we can clearly identify the direct excitation (at 0 fs delay) of the exciton S_3 feature at an energy of $E \approx 2.8$ eV above the kinetic energy E_H of the HOMO level. Shortly after the excitation, additional photoemission intensity builds up at $E - E_H \approx 2.0$ eV and ≈ 1.7 eV, which is known to be caused by relaxation to the S_2 and S_1 dark exciton states⁶ and is in good agreement with the theoretically predicted energies of $E - E_H \approx 2.1$ eV and ≈ 1.9 eV.

Changing now the pump photon energy to $h\nu = 3.6$ eV for direct excitation of the S_4 exciton band (Fig. 3c), two distinct peaks at ≈ 3.6 eV above the HOMO and the HOMO-1 are expected from theory. While photoemission intensity at $E - E_H \approx 3.6$ eV above the HOMO level is readily visible in Fig. 3c, the second feature at 3.6 eV above the HOMO-1 is expected at $E-E_H \approx 2.2$ eV above the HOMO level (corresponding to $E-E_{H-1}$ $\approx 3.6 \text{ eV}$) and thus almost degenerate with the aforementioned S₂ dark exciton band at about $E - E_H \approx 2.0$ eV, which appears after the optical excitation due to relaxation processes. Therefore, we need to pinpoint this second $H-1\rightarrow L$ contribution to the S_4 exciton at the earliest time of the excitation. Indeed, a closer look around 0 fs delay shows additional photoemission intensity at about $E - E_H \approx 2.2$ eV. Using difference maps (Fig. 3b) and direct comparisons of energy-distribution-curves at selected time-steps (Fig. 3d), we clearly find a double-peak structure corresponding to the energy difference of $\approx 1.4 \text{ eV}$ of the HOMO and HOMO-1 levels. Thereby, we have shown that photoelectron spectroscopy, in contrast to other techniques (e.g., absorption spectroscopy), is indeed able to disentangle different orbital contributions of the excitons. In this way, we have validated the theoretically predicted multi-peak structure of the multiorbital exciton state that is implied by Eq. (2). We also see that the photoelectron energies in the spectrum turn out to be sensitive probes of the corresponding hole contributions of the correlated exciton states.

We note that the signature of the S_3 excitons, even if not directly excited with the light

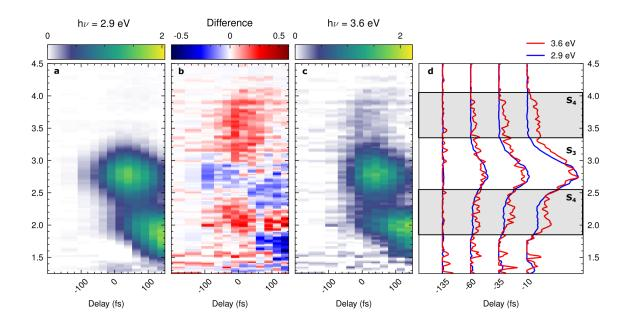


FIG. 3. **a-d**, comparison of the time-resolved photoelectron spectra of multilayer C₆₀ for $h\nu=2.9$ eV excitation and $h\nu=3.6$ eV excitation ((**a**) and (**c**), respectively), both normalized and shifted in time to match the intensity of the S₃ signals (see Methods for full details on the data analysis). As can be seen in the difference (**b**), for $h\nu=3.6$ eV pump we observe an enhancement of the photoemission yield around $E-E_H\approx3.6$ eV as well as around $E-E_H\approx2.2$ eV. We attribute this signal to the S₄ exciton band, which has hole contributions stemming from both the HOMO and the HOMO-1. To further quantify the signal of the S₄ exciton, (**d**) shows energy distribution curves for both measurements at early delays, showing the enhancement in the $h\nu=3.6$ eV measurement.

pulse in this measurement, is still visible and moreover with significantly higher intensity than the multiorbital signals of the resonantly excited S_4 exciton band. This observation strongly suggests that there is a very fast relaxation from the S_4 exciton to the S_3 exciton, with relaxation times well below 50 fs (see Extended Fig. 6).

D. Time-resolved photoemission orbital tomography of exciton wavefunctions

Based on the excellent agreement between the experiment and the GW+BSE theoretical results, we are now ready to investigate to what extent the momentum patterns from tr-POT data of excitons in organic semiconductors contain information about the real-space spatial

distribution of the exciton wavefunction. In the experiment, we once again excite the S_3 exciton band in the C_{60} film with $h\nu = 2.9$ eV pump energy, and we now use femtosecond tr-POT to collect the momentum fingerprints of the directly excited S₃ excitons around 0 fs and the subsequently built-up dark S_2 and S_1 excitons that appear in the exciton relaxation cascade in the C_{60} film (see Fig. 4a-c, where the momentum map of the lowest energy S_1 exciton band is plotted in (a), the S_2 in (b) and the highest energy S_3 exciton band in (c); see Extended Fig. 6 for time-resolved traces of the exciton formation and relaxation dynamics). We note that the collection of these data required integration times of up to 70 hours, and that a measurement of the comparatively low-intensity S_4 feature when excited with $h\nu = 3.6$ eV has not yet proved feasible. For the interpretation of the collected POT momentum maps from the S_1 , S_2 , and S_3 excitons, we also calculate the expected momentum fingerprints for the wavefunctions obtained from the GW+BSE calculation for both dimers, each rotated to all occurring orientations in the crystal. Finally, for the theoretical momentum maps, we sum up the photoelectron intensities of each electron-hole transition in an energy range of 200 meV centered on the exciton band. The results are shown in Fig. 4d-f below the experimental data for direct comparison.

First, we observe that the experimental momentum maps of the S_1 and S_2 states are largely similar (Fig. 4a,b), showing six lobes centered at $k_{\parallel} \approx 1.2 \text{ Å}^{-1}$. These features, as well as the energy splitting between S₁ and S₂ (cf. Fig. 2c), are accurately reproduced by the GW+BSE prediction (Fig. 4d,e). Furthermore, also the GW+BSE calculation shows very similar momentum maps for S_1 and S_2 , suggesting a similar spatial structure of the excitons. This is in contrast to a naive application of static POT to the unoccupied orbitals of the DFT ground state of C_{60} , which does show a similar momentum map for the LUMO, but cannot explain a kinetic energy difference in the photoemission signal, nor give any indication of differences in the corresponding exciton wavefunctions. With this agreement between experiment and theory, we now extract the spatial properties of the GW+BSEexciton wavefunctions. To visualize the degree of charge-transfer of these two-particle exciton wavefunctions $\psi_m(\mathbf{r_h}, \mathbf{r_e})$, we integrate the electron probability density over all possible hole positions r_h , considering only hole positions at one of the C_{60} molecules in the dimer. This effectively fixes the hole contribution to a particular C_{60} molecule (blue circles in Fig. 4g-i indicate the boundary of considered hole positions around one molecule, hole distribution not shown), and provides a probability density for the electronic part of the exciton wavefunction

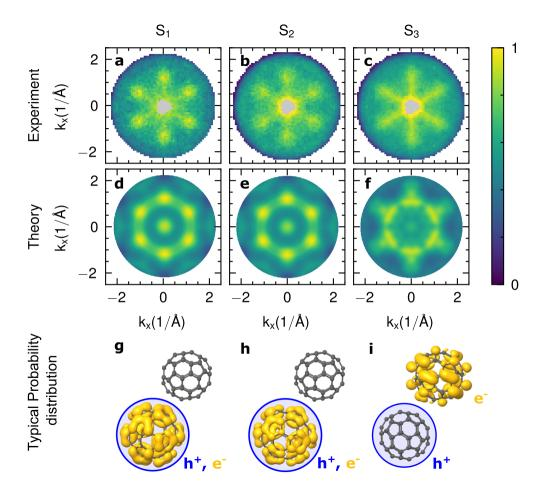


FIG. 4. **a-f**, comparison of the (**a-c**) experimental momentum maps acquired for the three exciton bands observed in C_{60} with the (**d-f**) predicted momentum maps retrieved from GW+BSE. Note that the center of the experimental maps could not be analyzed due to a space-charge-induced background signal in this region (gray area, see Methods). **g-i**, isosurfaces of the integrated electron probability density (yellow) within the 1-2 dimer for fixed hole positions on the bottom-left molecule (blue circle) of the dimer for the (**g**) S_1 , the (**h**) S_2 , and the (**i**) S_3 exciton bands.

in the dimer, which we visualize by a yellow isosurface (see Fig. 4g-i). Obviously, in the case of S_1 and S_2 (Fig. 4g,h), when the hole position is restricted to one molecule of the dimer, the electronic part of the exciton wavefunction is localized at the same molecule of the dimer. Our calculations thus suggest that the S_1 and S_2 excitons are of Frenkel-like nature. Their energy difference originates from different excitation symmetries possible for the $H\rightarrow L$ transition (namely t_{1g} , t_{2g} , and g_g for the S_1 and h_g for the S_2).¹²

In contrast to the S_1 and S_2 excitons, the momentum map of the S_3 band shows a much

more star-shaped POT fingerprint in both theory and experiment (Fig. 4c,f). This is to be expected, since the electronic part of the S_3 excitons contains not only contributions from the LUMO orbital, but also contributions from the LUMO+1 orbital. Note, however, that we find the experimentally observed star-shaped pattern to be only partially reproduced by the GW+BSE calculation. An indication towards the cause of this discrepancy is found by considering the electron-hole separation of the excitons making up the S₃ band. Here, we find that the positions of the electron and the hole contributions are strongly anticorrelated (Fig. 4i), with the electron confined to the neighboring molecule of the dimer. In fact, the mean electron-hole separation is as large as 7.6 Å, which is close to the core-to-core distance of the C₆₀ molecules. Although these theoretical results confirm the previouslyreported charge-transfer nature of the S_3 excitons^{5,6}, they also reflect the limitations of the C₆₀ dimer approach. Indeed, the dimer represents the minimal model to account for an intermolecular exciton delocalization effect, but it cannot fully account for dispersion effects²² (cf. Extended Fig. 5), which are required for a quantitative comparison with experimental data. Besides the discrepancy in the S₃ momentum map, this could also be an explanation why the S₂ in the present work is of Frenkel-like nature, but could have charge-transfer character according to previous studies^{5,6}. However, future developments will certainly allow scaling up of the cluster size in the calculation, so that exciton wavefunctions with larger electron-hole separation can be accurately described. Most importantly, we find that the present dimer GW+BSE calculations are clearly suited to elucidate the multiorbital character of the excitons, which is an indispensable prerequisite for the correct interpretation of tr-POT data of excitons in organic semiconductors.

III. CONCLUSION

In conclusion, we have shown how the energy- and momentum-resolved photoemission spectrum of excitons in an organic semiconductor depends on the multiorbital nature of these excitons. By extending POT to fully-interacting exciton states calculated in the framework of the Bethe-Salpeter equation, we found that the energy of the photoemitted electron of the exciton quasiparticle is determined by the position of the hole and the exciton energy in combination with the probe photon energy. This leads to the prediction of multiple peaks in the photoelectron spectrum, which we verify experimentally, and allows disentangling the differ-

ent orbital contributions, the wavefunction localization, and the charge-transfer character. Similarly, the momentum fingerprint provides access to the electron states that make up the exciton. Most importantly, we introduce time-resolved photoemission orbital tomography as a key technique for the study of exciton wavefunctions in organic semiconductors.

IV. ACKNOWLEDGEMENTS

This work was funded by the Deutsche Forschungsgemeinschaft (DFG, German Research Foundation) - 432680300/SFB 1456, project B01 and 217133147/SFB 1073, projects B07 and B10. G.S.M.J. acknowledges financial support by the Alexander von Humboldt Foundation. A.W., C.S.K., and P.P acknowledge support from the Austrian Science Fund (FWF) project I 4145. The computational results presented were achieved using the Vienna Scientific Cluster (VSC) and the local high-performance resources of the University of Graz. R.H., M.A., and B.S. acknowledge financial support by the DFG - 268565370/TRR 173, projects B05 and A02. B.S. acknowledges further support by the Dynamics and Topology Center funded by the State of Rhineland-Palatinate.

V. AUTHOR CONTRIBUTIONS

D.St., M.R., S.S., M.A., B.S., P.P., G.S.M.J. and S.M. conceived the research. W.B., D.Sch. and J.P.B. carried out the time-resolved momentum microscopy experiments. W.B. analyzed the data. W.B. and R.H. prepared the samples. A.W., C.S.K., G.D.A, X.B. and P.P. performed the calculations and analyzed the theoretical results. All authors discussed the results. G.S.M.J. and S.M. were responsible for the overall project direction and wrote the manuscript with contributions from all co-authors.

 $^{^{*}}$ gsmjansen@uni-goettingen.de

[†] smathias@uni-goettingen.de

Weijun Ke, Dewei Zhao, Corey R. Grice, Alexander J. Cimaroli, Jie Ge, Hong Tao, Hongwei Lei, Guojia Fang, and Yanfa Yan, "Efficient planar perovskite solar cells using room-temperature

- vacuum-processed C60 electron selective layers," Journal of Materials Chemistry A 3, 17971–17976 (2015), publisher: The Royal Society of Chemistry.
- Alain R. Puente Santiago, Tianwei He, Oscar Eraso, Md Ariful Ahsan, Aruna N. Nair, Venkata S. N. Chava, Ting Zheng, Srikanth Pilla, Olivia Fernandez-Delgado, Aijun Du, Sreeprasad T. Sreenivasan, and Luis Echegoyen, "Tailoring the Interfacial Interactions of van der Waals 1T-MoS2/C60 Heterostructures for High-Performance Hydrogen Evolution Reaction Electrocatalysis," Journal of the American Chemical Society 142, 17923–17927 (2020), publisher: American Chemical Society.
- ³ Zhenhua Yu, Zhibin Yang, Zhenyi Ni, Yuchuan Shao, Bo Chen, Yuze Lin, Haotong Wei, Zhengshan J. Yu, Zachary Holman, and Jinsong Huang, "Simplified interconnection structure based on C60/SnO2-x for all-perovskite tandem solar cells," Nature Energy 5, 657–665 (2020), number: 9 Publisher: Nature Publishing Group.
- ⁴ Yi Ming Wang, Prashant V. Kamat, and L. K. Patterson, "Aggregates of fullerene C60 and C70 formed at the gas-water interface and in DMSO/water mixed solvents. A spectral study," J. Phys. Chem. 97, 8793–8797 (1993).
- ⁵ Benjamin Stadtmüller, Sebastian Emmerich, Dominik Jungkenn, Norman Haag, Markus Rollinger, Steffen Eich, Mahalingam Maniraj, Martin Aeschlimann, Mirko Cinchetti, and Stefan Mathias, "Strong modification of the transport level alignment in organic materials after optical excitation," Nature Communications **10**, 1470 (2019), number: 1 Publisher: Nature Publishing Group.
- ⁶ Sebastian Emmerich, Sebastian Hedwig, Benito Arnoldi, Johannes Stöckl, Florian Haag, Ralf Hemm, Mirko Cinchetti, Stefan Mathias, Benjamin Stadtmüller, and Martin Aeschlimann, "Ultrafast Charge-Transfer Exciton Dynamics in C60 Thin Films," The Journal of Physical Chemistry C 124, 23579–23587 (2020), publisher: American Chemical Society.
- ⁷ Bret C. Hess, Don V. Bowersox, Shant H. Mardirosian, and Lawrence D. Unterberger, "Electroabsorption in C60 and C70. Third-order nonlinearity in molecular and solid states," Chemical Physics Letters 248, 141–146 (1996).
- ⁸ Martina Causa', Ivan Ramirez, Josue F. Martinez Hardigree, Moritz Riede, and Natalie Banerji, "Femtosecond Dynamics of Photoexcited C60 Films," J. Phys. Chem. Lett. 9, 1885–1892 (2018), publisher: American Chemical Society.

- Tobias Hahn, Steffen Tscheuschner, Christina Saller, Peter Strohriegl, Puttaraju Boregowda, Tushita Mukhopadhyay, Satish Patil, Dieter Neher, Heinz Bässler, and Anna Köhler, "Role of Intrinsic Photogeneration in Single Layer and Bilayer Solar Cells with C60 and PCBM," J. Phys. Chem. C 120, 25083–25091 (2016), publisher: American Chemical Society.
- Mufasila Mumthaz Muhammed, Junais Habeeb Mokkath, and Ali J. Chamkha, "Impact of packing arrangement on the optical properties of C60 cluster aggregates," Physical Chemistry Chemical Physics 24, 5946–5955 (2022), publisher: Royal Society of Chemistry.
- Junais Habeeb Mokkath, "Delocalized exciton formation in C60 linear molecular aggregates," Physical Chemistry Chemical Physics 23, 21901–21912 (2021), publisher: Royal Society of Chemistry.
- Hajime Kobayashi, Shinnosuke Hattori, Raku Shirasawa, and Shigetaka Tomiya, "Wannier-Like Delocalized Exciton Generation in C60 Fullerene Clusters: A Density Functional Theory Study," The Journal of Physical Chemistry C 124, 2379–2387 (2020), publisher: American Chemical Society.
- Peter Puschnig, Stephen Berkebile, Alexander J. Fleming, Georg Koller, Konstantin Emtsev, Thomas Seyller, John D. Riley, Claudia Ambrosch-Draxl, Falko P. Netzer, and Michael G. Ramsey, "Reconstruction of Molecular Orbital Densities from Photoemission Data," Science 326, 702–706 (2009).
- Matthijs Jansen, Marius Keunecke, Marten Düvel, Christina Möller, David Schmitt, Wiebke Bennecke, Jasmin Kappert, Daniel Steil, D. Russell Luke, Sabine Steil, and Stefan Mathias, "Efficient orbital imaging based on ultrafast momentum microscopy and sparsity-driven phase retrieval," New Journal of Physics (2020), 10.1088/1367-2630/ab8aae.
- ¹⁵ R. Wallauer, M. Raths, K. Stallberg, L. Münster, D. Brandstetter, X. Yang, J. Güdde, P. Puschnig, S. Soubatch, C. Kumpf, F. C. Bocquet, F. S. Tautz, and U. Höfer, "Tracing orbital images on ultrafast time scales," Science 371, 1056–1059 (2021), publisher: American Association for the Advancement of Science.
- Alexander Neef, Samuel Beaulieu, Sebastian Hammer, Shuo Dong, Julian Maklar, Tommaso Pincelli, R. Patrick Xian, Martin Wolf, Laurenz Rettig, Jens Pflaum, and Ralph Ernstorfer, "Orbital-resolved Observation of Singlet Fission," arXiv:2204.06824 [cond-mat] (2022), arXiv: 2204.06824.

- ¹⁷ K. Medjanik, O. Fedchenko, S. Chernov, D. Kutnyakhov, M. Ellguth, A. Oelsner, B. Schönhense, T. R. F. Peixoto, P. Lutz, C.-H. Min, F. Reinert, S. Däster, Y. Acremann, J. Viefhaus, W. Wurth, H. J. Elmers, and G. Schönhense, "Direct 3D mapping of the Fermi surface and Fermi velocity," Nature Materials 16, 615–621 (2017).
- Marius Keunecke, Christina Möller, David Schmitt, Hendrik Nolte, G. S. Matthijs Jansen, Marcel Reutzel, Marie Gutberlet, Gyula Halasi, Daniel Steil, Sabine Steil, and Stefan Mathias, "Time-resolved momentum microscopy with a 1 MHz high-harmonic extreme ultraviolet beamline," Review of Scientific Instruments 91, 063905 (2020), publisher: American Institute of Physics.
- Marius Keunecke, Marcel Reutzel, David Schmitt, Alexander Osterkorn, Tridev A. Mishra, Christina Möller, Wiebke Bennecke, G. S. Matthijs Jansen, Daniel Steil, Salvatore R. Manmana, Sabine Steil, Stefan Kehrein, and Stefan Mathias, "Electromagnetic dressing of the electron energy spectrum of Au(111) at high momenta," Physical Review B 102, 161403 (2020).
- Haiqian Wang, Changgan Zeng, Bing Wang, J. G. Hou, Qunxiang Li, and Jinlong Yang, "Orientational configurations of the C 60 molecules in the (2 × 2) superlattice on a solid C 60 (111) surface at low temperature," Physical Review B 63, 085417 (2001).
- M.S. Dresselhaus, G. Dresselhaus, and P.C. Eklund, "Chapter 12 electronic structure," in Science of Fullerenes and Carbon Nanotubes, edited by M.S. Dresselhaus, G. Dresselhaus, and P.C. Eklund (Academic Press, San Diego, 1996) pp. 413–463.
- Norman Haag, Daniel Lüftner, Florian Haag, Johannes Seidel, Leah L. Kelly, Giovanni Zamborlini, Matteo Jugovac, Vitaliy Feyer, Martin Aeschlimann, Peter Puschnig, Mirko Cinchetti, and Benjamin Stadtmüller, "Signatures of an atomic crystal in the band structure of a \${\mathbb{C}}_{60}\$ thin film," Phys. Rev. B **101**, 165422 (2020), publisher: American Physical Society.
- ²³ Martin Weinelt, Michael Kutschera, Thomas Fauster, and Michael Rohlfing, "Dynamics of Exciton Formation at the Si(100) c(4 × 2) Surface," Phys. Rev. Lett. **92**, 126801 (2004), publisher: American Physical Society.
- Shuo Dong, Michele Puppin, Tommaso Pincelli, Samuel Beaulieu, Dominik Christiansen, Hannes Hübener, Christopher W. Nicholson, Rui Patrick Xian, Maciej Dendzik, Yunpei Deng, Yoav William Windsor, Malte Selig, Ermin Malic, Angel Rubio, Andreas Knorr, Martin Wolf, Laurenz Rettig, and Ralph Ernstorfer, "Direct measurement of key exciton properties: Energy,

- dynamics, and spatial distribution of the wave function," Natural Sciences 1, e10010 (2021), type: Journal Article.
- Robert Wallauer, Raul Perea-Causin, Lasse Münster, Sarah Zajusch, Samuel Brem, Jens Güdde, Katsumi Tanimura, Kai-Qiang Lin, Rupert Huber, Ermin Malic, and Ulrich Höfer, "Momentum-Resolved Observation of Exciton Formation Dynamics in Monolayer WS2," Nano Lett. 21, 5867–5873 (2021), publisher: American Chemical Society.
- Julien Madéo, Michael K. L. Man, Chakradhar Sahoo, Marshall Campbell, Vivek Pareek, E. Laine Wong, Abdullah Al-Mahboob, Nicholas S. Chan, Arka Karmakar, Bala Murali Krishna Mariserla, Xiaoqin Li, Tony F. Heinz, Ting Cao, and Keshav M. Dani, "Directly visualizing the momentum-forbidden dark excitons and their dynamics in atomically thin semiconductors," Science 370, 1199–1204 (2020).
- David Schmitt, Jan Philipp Bange, Wiebke Bennecke, AbdulAziz AlMutairi, Giuseppe Meneghini, Kenji Watanabe, Takashi Taniguchi, Daniel Steil, D. Russell Luke, R. Thomas Weitz, Sabine Steil, G. S. Matthijs Jansen, Samuel Brem, Ermin Malic, Stephan Hofmann, Marcel Reutzel, and Stefan Mathias, "Formation of moiré interlayer excitons in space and time," Nature 608, 499–503 (2022).
- Daria Popova-Gorelova, Jochen Küpper, and Robin Santra, "Imaging electron dynamics with time- and angle-resolved photoelectron spectroscopy," Phys. Rev. A 94, 013412 (2016).
- ²⁹ Umberto De Giovannini, Hannes Hübener, and Angel Rubio, "A First-Principles Time-Dependent Density Functional Theory Framework for Spin and Time-Resolved Angular-Resolved Photoelectron Spectroscopy in Periodic Systems," Journal of Chemical Theory and Computation 13, 265–273 (2017).
- ³⁰ Sebastian Hammon and Stephan Kümmel, "Pump-probe photoemission simulated in real time: Revealing many-particle signatures," Physical Review A 104, 012815 (2021).
- Marvin Reuner and Daria Popova-Gorelova, "Attosecond imaging of photoinduced dynamics in molecules using time-resolved photoelectron momentum microscopy," Phys. Rev. A 107, 023101 (2023).
- ³² Christian Kern, Andreas Windischbacher, and Peter Puschnig, "Photoemission orbital tomography of excitons," unpublished.
- M. Dauth, M. Wiessner, V. Feyer, A. Schöll, P. Puschnig, F. Reinert, and S. Kümmel, "Angle resolved photoemission from organic semiconductors: orbital imaging beyond the molecular

- orbital interpretation," New J. Phys. 16, 103005 (2014).
- ³⁴ X. Y. Zhu, "How to draw energy level diagrams in excitonic solar cells," The Journal of Physical Chemistry Letters , 2283–2288 (2014).
- B. Schönhense, K. Medjanik, O. Fedchenko, S. Chernov, M. Ellguth, D. Vasilyev, A. Oelsner, J. Viefhaus, D. Kutnyakhov, W. Wurth, H. J. Elmers, and G. Schönhense, "Multidimensional photoemission spectroscopy—the space-charge limit," New Journal of Physics 20, 033004 (2018), publisher: IOP Publishing.
- Richard M. David, William I. F.and Ibberson, Judy C. Matthewman, Kosmas Prassides, T. John S. Dennis, Jonathan P. Hare, Harold W. Kroto, Roger Taylor, and David R. M. Walton, "Crystal structure and bonding of ordered c60," Nature 353, 147–149 (1991).
- W. I. F. David, R. M. Ibberson, T. J. S. Dennis, J. P. Hare, and K. Prassides, "Structural phase transitions in the fullerene c60," Europhysics Letters 18, 219 (1992).
- R. Krishnan, J. S. Binkley, R. Seeger, and J. A. Pople, "Self-consistent molecular orbital methods. xx. a basis set for correlated wave functions," The Journal of Chemical Physics 72, 650–654 (1980), https://doi.org/10.1063/1.438955.
- Michael J. Frisch, John A. Pople, and J. Stephen Binkley, "Self-consistent molecular orbital methods 25. supplementary functions for gaussian basis sets," The Journal of Chemical Physics 80, 3265–3269 (1984), https://doi.org/10.1063/1.447079.
- ⁴⁰ Carlo Adamo and Vincenzo Barone, "Toward reliable density functional methods without adjustable parameters: The pbe0 model," The Journal of Chemical Physics 110, 6158–6170 (1999), https://doi.org/10.1063/1.478522.
- Stefan Grimme, Jens Antony, Stephan Ehrlich, and Helge Krieg, "A consistent and accurate ab initio parametrization of density functional dispersion correction (dft-d) for the 94 elements h-pu," The Journal of Chemical Physics 132, 154104 (2010), https://doi.org/10.1063/1.3382344.
- ⁴² Frank Neese, "The ORCA program system," Wiley Interdisciplinary Reviews: Computational Molecular Science 2, 73–78 (2012).
- 43 Frank Neese. "Software update: The program system—version orca 5.0," WIREs Computational Molecular Science **12**, e1606(2022),https://wires.onlinelibrary.wiley.com/doi/pdf/10.1002/wcms.1606.
- Denis Jacquemin, Ivan Duchemin, and Xavier Blase, "Is the Bethe–Salpeter Formalism Accurate for Excitation Energies? Comparisons with TD-DFT, CASPT2, and EOM-CCSD," J.

- Phys. Chem. Lett. 8, 1524–1529 (2017).
- ⁴⁵ Gabriele D'Avino, Luca Muccioli, Claudio Zannoni, David Beljonne, and Zoltán G. Soos, "Electronic polarization in organic crystals: A comparative study of induced dipoles and intramolecular charge redistribution schemes," Journal of Chemical Theory and Computation 10, 4959–4971 (2014), pMID: 26584380, https://doi.org/10.1021/ct500618w.
- Jing Li, Gabriele D'Avino, Ivan Duchemin, David Beljonne, and Xavier Blase, "Combining the many-body gw formalism with classical polarizable models: Insights on the electronic structure of molecular solids," The Journal of Physical Chemistry Letters 7, 2814–2820 (2016), pMID: 27388926, https://doi.org/10.1021/acs.jpclett.6b01302.
- ⁴⁷ Jing Li, Gabriele D'Avino, Anton Pershin, Denis Jacquemin, Ivan Duchemin, David Beljonne, and Xavier Blase, "Correlated electron-hole mechanism for molecular doping in organic semi-conductors," Phys. Rev. Materials 1, 025602 (2017).
- Sheng Dai, L. Mac Toth, G. D. Del Cul, and David H. Metcalf, "Ultraviolet-visible absorption spectrum of C60 vapor and determination of the C60 vaporization enthalpy," J. Chem. Phys. 101, 4470–4471 (1994), publisher: American Institute of Physics.
- ⁴⁹ Shinji Hasegawa, Takayuki Miyamae, Kyuya Yakushi, Hiroo Inokuchi, Kazuhiko Seki, and Nobuo Ueno, "Origin of the photoemission intensity oscillation of c₆₀," Phys. Rev. B **58**, 4927–4933 (1998).

VI. METHODS

A. Femtosecond momentum microscopy of $C_{60}/Cu(111)$

We apply full multidimensional time- and angle-resolved photoelectron spectroscopy (tr-ARPES) to a multilayer C_{60} crystal evaporated onto Cu(111), where the film thickness was such that no photoemission signature of the underlying Cu(111) could be observed in our experiment. We verified the sample quality by performing momentum microscopy of the occupied HOMO and HOMO-1 states simultaneously to the measurement of the excited states (see Extended Fig. 5). Femtosecond exciton dynamics were induced using ≈ 100 fs, $h\nu = 2.9 \text{ eV}$ or $\approx 100 \text{ fs}$, $h\nu = 3.6 \text{ eV}$ laser pulses derived from the frequency-doubled output of a optical parametric amplifier. The exciton dynamics were probed using our custom photoemission momentum microscope with a 500 kHz ultrafast 26.5 eV extreme ultraviolet (EUV) light source¹⁸ that enables us to map the photoelectron momentum distribution over the full photoemission horizon in a kinetic energy range exceeding 6 eV and an overall time resolution of ≈ 100 fs (the EUV pulse length is about 20 fs). The pump fluence was set to $90(10) \mu J/cm^2$ and $20(5) \mu J/cm^2$ for the $h\nu = 2.9 \text{ eV}$ and the $h\nu = 3.6 \text{ eV}$ measurement, respectively. To prevent the free rotation of C₆₀ molecules, we cooled the sample down to $\approx \! 80 \; \mathrm{K}^{20}.$ In addition to the resulting long-range periodic ordering of the C_{60} crystal, cooling was also observed to prevent light-induced polymerization.

B. Momentum microscopy data analysis

1. Space-charge effects

In the momentum microscopy experiment, a balance has to be found between sufficiently low pump and probe light intensities to avoid space-charge effects, but also having sufficient intensity for the optical excitation (pump) and reasonably short integration times (probe). Most of the time, for our settings, small space-charge effects are present in the data, but do not lead to strong distortions in the band-structure data and can be easily corrected. Therefore, the first step in the data analysis was to subtract a space-charge-induced delayand momentum-dependent kinetic energy shift. For this purpose, the central kinetic energy of the HOMO was determined for normalization. To avoid the influence of the C_{60} crystal

band structure²², we fitted a two-dimensional Lorentzian³⁵ and shifted the kinetic energy distribution accordingly, leading to the expected overall flat shape of the molecular orbitals in the ARPES data.

2. Replicas from the 13th harmonic

Although we use narrow-band multilayer mirrors to select the $11^{\rm th}$ harmonic at $h\nu=26.5~{\rm eV}$ from our laser-based high-harmonic generation spectrum¹⁸, we observe subtle replicas of the HOMO, HOMO-1, and HOMO-2 states in the unoccupied regime of the spectrum that are caused by photoemission from the $13^{\rm th}$ harmonic at at $h\nu=31.2~{\rm eV}$. To quantify these replica signals, we fitted the static reference spectrum above $E-E_H=1.2~{\rm eV}$ (i.e., in the unoccupied regime of the spectrum) with three Gaussian-shaped peaks for the HOMO replicas and an exponential function to account for residual photoemission intensity in the unoccupied regime that is caused in this spectral region by the much stronger direct $11^{\rm th}$ harmonic one-photon-photoemission from the HOMO state. After carrying out this fitting routine, we are able to calculate clean $11^{\rm th}$ harmonic spectra (static and time-resolved) via subtraction of the fitted $13^{\rm th}$ harmonic HOMO replicas. Note that we only subtract the replica signals, but not the background signal that is caused by one-photon-photoemission with the $11^{\rm th}$ harmonic from the HOMO state, because this background is time-dependent⁵, and needs to be explicitly considered in the fitting procedure. The data shown in Fig. 3 of the main text is processed in the way described above.

3. Fitting procedure for the time-resolved data

From replica-free trPES data for $h\nu = 2.9$ eV excitation, we determine the amplitude A_i , kinetic energy E_i , and bandwidth ΔE_i for the i^{th} exciton signature using a global fitting

approach. In particular, we apply the model

$$I(E,t) = \frac{A_{S_3}(t)}{\sqrt{2\pi}\Delta E_{S_3}} \exp\left[(E - E_{S_3}(t))^2/\Delta E_{S_3}^2\right] + \frac{A_{S_2}(t)}{\sqrt{2\pi}\Delta E_{S_2}} \exp\left[(E - E_{S_2})^2/\Delta E_{S_2}^2\right] + \frac{A_{S_1}(t)}{\sqrt{2\pi}\Delta E_{S_1}} \exp\left[(E - E_{S_1})^2/\Delta E_{S_1}^2\right] + A_{bg}(t) * \exp\left[-E/\tau\right].$$
(3)

Here, the last term is needed to account for the above-mentioned delay-dependent photoemission intensity that is caused by a transient renormalization of the HOMO state, as found in Ref. 5.

The fit results of this model applied to the $h\nu=2.9$ eV excitation and momentum-integrated data are shown in Table I, and Extended Fig. 6a for the time-resolved exciton dynamics.

Exciton	Kin. Energy (eV)	Bandwidth (FWHM) (eV)
S_3 (t=0 fs)	2.768(2)	0.606(4)
S_2	1.978(2)	0.406(3)
S_1	1.667(1)	0.362(2)

TABLE I. Peak parameters for $h\nu = 2.9$ eV excitation, extracted using Eq. 3. Note that we give the full width at half maximum (FWHM) for the bandwidth.

For the measurement with $h\nu = 3.6$ eV excitation, we account for the S₄ exciton band by extending the model in Eq. 3 with a set of Gaussian peaks with identical temporal evolution, given by

$$I(E,t) = \dots + \frac{A_{S_4}(t)}{2\sqrt{2\pi}\Delta E_{S_4}} \left(\exp\left[(E - E_{S_4,upper})^2/\Delta E_{S_4}^2\right] + \exp\left[(E - E_{S_4,lower})^2/\Delta E_{S_4}^2\right]\right),\tag{4}$$

which follows the same notation as Eq. 3. Here, we set $E_{S_4,upper}$ to be close to 3.6 eV, and following the GW+BSE calculation we set $E_{S_4,upper}-E_{S_4,lower}=1.4$ eV. Fitting this model to the momentum-integrated $h\nu=3.6$ eV excitation data, we find $E_{S_4,upper}=3.59(1)$ eV, and for the FWHM of the S₄ we find 0.58(3) eV. The time-resolved amplitudes retrieved

using this model are shown in Extended Fig. 6b. Furthermore, this analysis was used in Fig. 3 of the main text to subtract the exponential background $A_{bg}(t) * \exp[-E/\tau]$ related to the transient broadening of the HOMO state.

4. Fitting procedure for the time- and momentum-resolved data

In order to analyze the time-resolved data also momentum-resolved and thereby retrieve the momentum patterns that are shown in Fig. 1 and Fig. 4 in the main text, we carry out the fitting routine separately for pixel-resolved energy-distribution curves in the momentum distribution (1 pixel corresponds to $\approx 0.02 \text{ Å}^{-2}$). To optimize the signal-to-noise ratio, we apply a three-fold rotational symmetrization and a mirror symmetrization that match with crystal symmetry. Nevertheless, the signal-to-background ratio in a small region around the center of the photoemission horizon remains below 1, and we therefore exclude this region in our analysis (grey areas in Fig. 4 in the main text). Also, for the momentum-resolved data, the replica HOMO background signals due to the 13th harmonic amounts to 0, 1 or at most 2 counts in the pixel-resolved (momentum-resolved) energy-distribution curves, and can therefore not be fitted and subtracted accurately as described above for the momentumintegrated data. As such, we need to ignore the HOMO replicas from the 13th harmonic in the momentum-resolved analysis. We avoid overfitting of the model in Eq. 3 by fixing the energy and bandwidth of the peaks in the fitting routine to the parameters given in Table I. Thus, the set of free parameters in the momentum-resolved fitting procedure is limited to $A_{S_3}(k)$, $A_{S_2}(k)$, $A_{S_1}(k)$ and $A_{bg}(k)$. This approach enables the extraction of reliable momentum distributions also for the partially overlapping energy distributions of the S_1 and S_2 . The 1σ errors for the full momentum maps are shown in Extended Fig. 7.

We note that the overall photoemission intensity of the S_4 peak in the $h\nu=3.6$ eV excitation data is comparably low due to the sub-50 fs decay to the lower-energy S_3 excitons (see Fig. 3 in main text, Extended Fig. 6b). Furthermore, with $h\nu=3.6$ eV excitation, two-photon photoemission with 2*3.6 eV = 7.2 eV is sufficient to overcome the work function, so that space-charge effects could only be avoided by considerably reducing the $h\nu=3.6$ eV pump intensity. Therefore, the signal-to-noise ratio in these measurements was not sufficient for a momentum-resolved analysis of the S_4 exciton data.

C. Calculation of the C_{60} exciton spectrum

The ab initio calculation of the exciton spectrum of the C_{60} film was performed in two steps, using a GW+BSE approach. For the static electronic structure, we perform calculations for two unique C₆₀ dimers, which have been extracted from the known structure of the molecular film^{36,37} (see Fig. 2c, dimers 1-2 and 1-4 respectively). Starting from Kohn-Sham orbitals and energies of a ground state DFT calculation (6-311G*/PBE0+D3)³⁸⁻⁴¹ using ORCA 5.0.1^{42,43}, we employ the Fiesta code⁴⁴ to self-consistently correct the molecular energy levels by quasi-particle self-energy calculations with the GW approximation. To account for polarization effects beyond the molecular dimer, we embed the dimer cluster in a discrete polarizable model using the MESCal program^{45–47}. We found that mimicking 2 layers of the surrounding C_{60} film in such a way resulted in the convergence of the band gap within 0.1 eV with a removal energy from the highest valence level of 6.65 eV. The close agreement of this quasi-particle energy with the experimentally determined work function of 6.5 eV gives us additional confidence in the choice of our embedding environment. The calculated quasi-particle energy levels are shown in Fig. 2a. Here the finite width of the black bars actually arises from multiple energy levels forming bands on the energy axis. We characterize them according to symmetry²¹ as HOMO-1, HOMO, LUMO, and LUMO+1 bands, each consisting of 18, 10, 6 and 6 energy levels per dimer, respectively. Note that we combine HOMO-1 is made up by states from two different irreducible representations of the isolated gas phase C_{60} molecule which are practically forming a single band.

Building upon the GW energies, we compute neutral electron-hole excitations by solving the Bethe-Salpeter equation beyond the Tamm-Dancoff approximation (TDA). This yields the excitation energies Ω_m and the electron-hole coupling coefficients $X_{vc}^{(m)}$ for a series of excitons labelled with m. We first analyze the resulting optical absorption spectrum which is shown in Fig. 2c as black solid line. It reveals a prominent absorption band around $h\nu = 3.6$ eV that is well-known from gas-phase spectroscopy⁴⁸. Secondly, the dimer calculation reveals a strong optical absorption at $h\nu = 2.8$ eV as well as a weakly dipole-allowed transition at $h\nu = 2$ eV. Both of these transitions are known to only appear in aggregated phases of C_{60}^4 , and cannot be understood by considering only a single C_{60} molecule. We refer to the exciton bands around $\Omega = 1.9, 2.1, 2.8$ and 3.6 eV as S_1 , S_2 , S_3 and S_4 , respectively.

In line with our classification of the GW energy levels, one can group the composition of

the excitons into four categories according to the contributing quasi-particle energy levels. As visualized in Fig. 2c, this shows that S_1 and S_2 are almost completely described by HOMO to LUMO transitions. On the other hand, S_3 is predicted to have a small contribution of HOMO-1 character, however this contribution is too small to be reliably measured in our experiment. Finally, for S_4 we observe a clear and almost equal mixture of HOMO-1 and HOMO contributions, which is also confirmed by our measurements. Contributions from lower lying valence bands are negligibly small in the studied energy window.

D. Calculation of the exciton momentum maps

Based on our Kohn-Sham orbitals and BSE excitation coefficients, we calculate theoretical momentum maps for each exciton according to Eq. 2 following the derivation of Kern et al.³². Note that for better readability, Eqs. (1) and (2) are given within the TDA, however, can in general be extended to include also de-excitation terms.³² In the present case, we found the de-excitation contributions to be marginal (below 1%) without affecting the appearance of the momentum maps and our interpretation. The energy conservation term comprises the BSE excitation energies (Ω_m) , the GW quasi-particle energies for electron removal (i.e. ionization potential ε_v), and the probe energy of $h\nu = 26.5$ eV in accordance with our experimental setup. Furthermore, we include an inner potential to correct for the photoemission intensity variation of 3D molecules along the moment vector component perpendicular to the surface. Here, we choose a value of 12.5 eV, which has already been shown to match with experimental C_{60} data^{22,49}. (Note that while considering the inner potential of the film is essential to describe the ARPES fingerprint, a variation of the inner potential between 12 and 14 eV indicated no influence on the interpretation of our results.) As we exploited the plane-wave approximation, the calculated photoemission intensity is modulated by the momentum-dependent polarization factor $|\mathbf{A} \cdot \mathbf{k}|$, which we modelled as p-polarized light incoming with 68° to the surface normal according to experiments. To account for the symmetry of the C_{60} film, the momentum maps were 3-fold rotated and mirrored. Finally, application of Eq. 2 provides us with a 4D data set of simulated photoemission intensity as a function of the excitation energy (Ω_m) , the kinetic energy (E_{kin}) and the momentum components k_x and k_y . Analogous to experiment, we referenced the kinetic energy against the energy of the HOMO. The calculated ionization potential was further used to set the photoemission horizon of the theoretical momentum maps. Finally, to arrive at the theoretical momentum maps shown in Fig. 4, we sum up the photoelectron intensities of each contributing electron-hole transition in an kinetic energy range of 200 meV centered on the respective exciton band.

VII. EXTENDED FIGURES

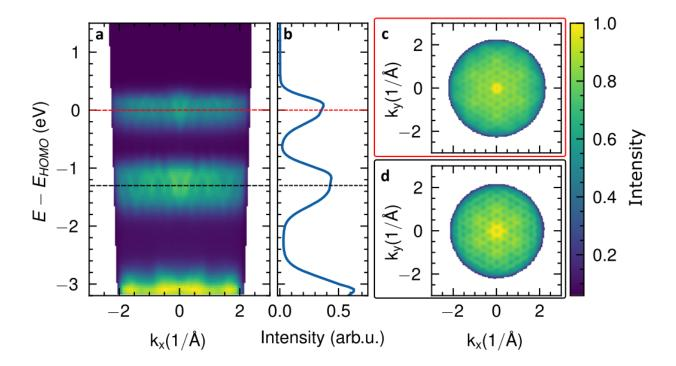


FIG. 5. Static photoelectron momentum microscopy of the multilayer C_{60} sample, taken from the time-resolved data at -1000 fs. The high contrast and line shape of the occupied molecular orbitals as shown in the energy-momentum cut (a) and integrated energy distribution curve (b) confirm that an influence of the Cu(111) substrate can be ignored. **c**, **d**: Furthermore, the clear modulation of the HOMO (c) and HOMO-1 (d) momentum maps confirm the high crystallinity of the multilayer at 80 K^{22}

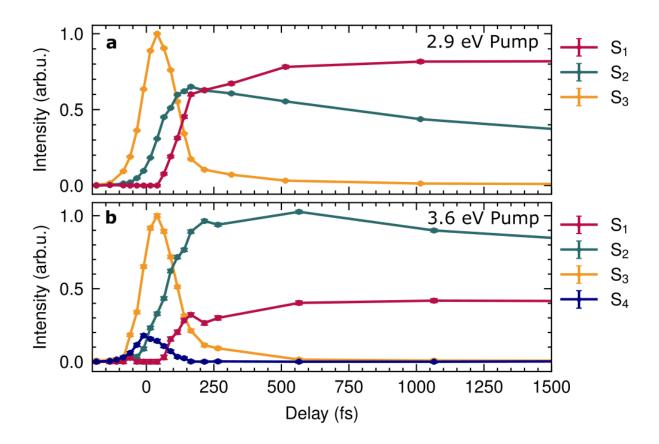


FIG. 6. **a, b:** Exciton-resolved measurement of the femtosecond relaxation dynamics after $h\nu=2.9$ and $h\nu=3.6$ eV excitation, respectively. The relative intensities were acquired by fitting the model in Eq. 3 and 4 to the momentum-integrated trPES data. Analysis of the time dependence indicates a sub 50 fs lifetime of the S₄ states. The comparably large S₂ population in the $h\nu=3.6$ eV measurement can potentially be explained by a relaxation of the S₄ into both the S₃ and S₂ states.

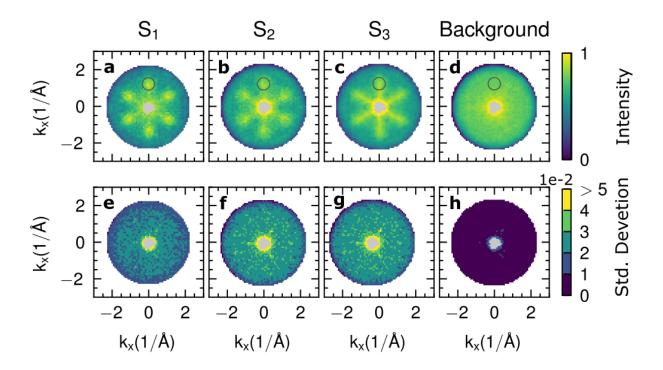


FIG. 7. Amplitude $(\mathbf{a}, \mathbf{b}, \mathbf{c}, \mathbf{d})$ and standard deviation $(\mathbf{e}, \mathbf{f}, \mathbf{g}, \mathbf{h})$ of the extracted momentum maps of the S_1 , S_2 , S_3 and the exponential background $(A_{bg}(k))$, respectively. The data are scaled to the mean value inside the circled area.